The Heated Condensation Framework. Part I: Description and Southern Great Plains Case Study

AHMED B. TAWFIK* AND PAUL A. DIRMEYER

Center for Ocean–Land–Atmosphere Studies, George Mason University, Fairfax, Virginia

JOSEPH A. SANTANELLO JR.

Hydrological Sciences, NASA Goddard Space Flight Center, Greenbelt, Maryland

(Manuscript received 23 June 2014, in final form 1 May 2015)

ABSTRACT

This study extends the heated condensation framework (HCF) presented in Tawfik and Dirmeyer to include variables for describing the convective background state of the atmosphere used to quantify the contribution of the atmosphere to convective initiation within the context of land–atmosphere coupling. In particular, the ability for the full suite of HCF variables to 1) quantify the amount of latent and sensible heat energy necessary for convective initiation, 2) identify the transition from moistening advantage to boundary layer growth advantage, 3) identify locally originating convection, and 4) compare models and observations, directly highlighting biases in the convective state, is demonstrated. These capabilities are illustrated for a clear-sky and convectively active day over the Atmospheric Radiation Measurement Program Southern Great Plains central station using observations, the Rapid Update Cycle (RUC) operational model, and the North American Regional Reanalysis (NARR). The clear-sky day had a higher and unattainable convective threshold, making convective initiation unlikely. The convectively active day had a lower threshold that was attained by midafternoon, reflecting local convective triggering. Compared to observations, RUC tended to have the most difficulty representing the convective state and captured the threshold for the clear-sky case only because of compensating biases in the moisture and temperature profiles. Despite capturing the observed moisture profile very well, a stronger surface inversion in NARR returned overestimates in the convective threshold. The companion paper applies the HCF variables introduced here across the continental United States to examine the climatological behavior of convective initiation and local land–atmosphere coupling.

1. Introduction

The representation of convective cloud cover and precipitation is one of the principle uncertainties in climate models (Dai 2006; Liang 2004; Song et al. 2013; DeAngelis et al. 2013). This is due in part to the small scales relative to model grid size at which convection occurs and the complex interactions between large-scale forcings and local surface conditions on subdiurnal time scales (e.g., Zhang 2003; Weaver 2004; Frye and Mote 2010; Lintner et al. 2013; Trier et al. 2013; Ruiz-Barradas and Nigam 2013). To properly understand and capture these complex interactions, relationships between the various scales from the land surface (e.g., local) to the atmosphere (e.g., background state) must be consistently quantified.

Traditionally, two approaches have been taken when exploring the impacts of the land surface on precipitation. The first attempts to capture the bulk interaction between soil moisture and precipitation essentially quantified the time-averaged or aggregate interactions (e.g., Fennessy and Shukla 1999; Findell and Eltahir 2003a; Koster et al. 2006, 2009; Dirmeyer 2006; Findell et al. 2011). The first phase of the Global Land–Atmosphere Coupling Experiment (GLACE) suggested that semiarid–semihumid regions favor a positive soil moisture–precipitation feedback, meaning wet soil moisture anomalies favor an increase in precipitation

* Current affiliation: Climate and Global Dynamics, National Center for Atmospheric Research, Boulder, Colorado.

Corresponding author address: Ahmed Tawfik, Climate and Global Dynamics, National Center for Atmospheric Research, 1850 Table Mesa Drive, Boulder, CO 80305.
E-mail: abtawfik@ucar.edu

DOI: 10.1175/JHM-D-14-0117.1

© 2015 American Meteorological Society

(Koster et al. 2004). It should be noted that the variations in the strength of coupling across the participating models were large (Guo et al. 2006; Dirmeyer et al. 2006). Following similar experiment designs, several regional modeling studies identified hotspots in semi-arid regions (Seneviratne et al. 2006; Zhang et al. 2008; Tawfik and Steiner 2011; Mei and Wang 2012); however, the location of modeled arid–humid transitions can vary depending on the land surface and atmospheric model coupling combination.

The second approach attempts to disaggregate coupling among the various process links that connect soil moisture to precipitation (e.g., Ek and Holtslag 2004; Betts 2009; Santanello et al. 2009, 2011; Seneviratne et al. 2010; van Heerwaarden et al. 2010; Dirmeyer 2011; Ferguson et al. 2012). A valuable tool for dissecting the relative contributions of surface fluxes to boundary layer development is the mixing diagram approach (Betts 1984, 1992; Santanello et al. 2009). Mixing diagrams use the diurnal coevolution of 2-m temperature and humidity to identify the influence of local surface energy fluxes on boundary layer development. Santanello et al. (2013) present a comprehensive mixing diagram analysis comparing nine combinations of land surface and boundary layer schemes in the NASA Land Information System (LIS) coupled to the Weather Research and Forecasting (WRF) Model against observations over the Atmospheric Radiation Measurement Program (ARM) Southern Great Plains (SGP) stations. They showed that the sensitivity of planetary boundary layer (PBL) development to changes in soil moisture initialization varied depending on the combination of land surface and PBL parameterization. Using a single-column boundary layer model with a quasi-analytical solution for relative humidity at the top of the PBL, modified from Ek and Holtslag (2004), Gentine et al. (2013) found that convective initiation over land is determined by several interrelated factors: surface evaporative fraction, surface temperature, relative humidity of the free troposphere, and the ratio of moisture and temperature lapse rates in the free troposphere. This results in two distinct regimes capable of triggering convection, a dry regime where boundary layer growth increases relative humidity at the top of the boundary layer and a wet regime where surface moisture inputs under a strong inversion directly increase boundary layer humidity. This is in agreement with observational studies that also used the Ek and Holtslag (2004) methodology to show the existence of a dry boundary layer growth regime (Westra et al. 2012).

Much attention has also been dedicated to addressing the well-known early diurnal onset of parameterized convective precipitation in models (e.g., Ghan et al. 1996; Dai et al. 1999; Zhang 2003; Collier and Bowman 2004; Dai and Trenberth 2004; Rosa and Collins 2013; Hohenegger and Stevens 2013a) and its connection with surface fluxes (Zhang 2003; Guichard et al. 2004; Chaboureau et al. 2004; Lee et al. 2010). By evaluating the time derivative of convective available potential energy (CAPE), Zhang (2003) was able to show that surface fluxes were out of phase with the diurnal precipitation maximum over the SGP and that large-scale forcings were likely controlling the observed nighttime precipitation maximum. Ruiz-Barradas and Nigam (2013) showed similar results over the SGP region, implicating low-level moisture transport as the primary driver of precipitation. Additionally, using 13 yr of observations, Zhang and Klein (2013) found that boundary layer relative humidity was enhanced during active nonprecipitating shallow cumulus development typically produced by high morning evaporative fraction locally and horizontal moisture advection below 850 hPa. This was consistent with previous work that found the transition from shallow to deep convection to be positively correlated with greater moisture above the boundary layer (Zhang and Klein 2010).

Examining the conditions favorable for the development of deep convection over the tropical Atlantic Ocean, Hohenegger and Stevens (2013b) showed that moisture convergence is a more dominant mechanism for initiating deep convection than local surface flux forcing. Estimates relating this analysis to typical ARM-SGP conditions returned similar results, highlighting the importance of nonlocal moisture transport (Hohenegger and Stevens 2013c). Prior work has attempted to relate early morning conditions to afternoon precipitation (Findell and Eltahir 2003a,b), demonstrating that convection may be initiated over either anomalously wet or dry soils depending on the overlying atmosphere. Ferguson and Wood (2011) found this framework to be latitudinally dependent when applied globally. Additionally, satellite-based estimates have suggested weaker coupling than many modeling studies (Ferguson et al. 2012; Taylor et al. 2012). Using the North American Regional Reanalysis (NARR), Findell et al. (2011) found a positive feedback relationship between morning evaporative fraction and the triggering of afternoon precipitation over the southeastern United States, but no significant correlation over the central United States. This result was found to be most significant in the summer when the methodology of Findell et al. (2011) was applied to the entire seasonal cycle (Berg et al. 2013).

Although some of these studies appear to downplay the importance of surface fluxes and surface energy

TABLE 1. Summary description of the HCF diagnostic variables.

Name	Description	Calculation
BCL	Buoyant condensation level; saturation height due to buoyant mixing only	See Fig. 1
θ_{BM}	Buoyant mixing potential temperature; θ_{2m} needed to reach the BCL	Descend from BCL to surface
PML	Potential mixed level; height where perturbed θ_{2m} is neutrally buoyant	θ_{2m} intersects θ profile
q_{mix}	Specific humidity of the potential mixed layer	Mix q profile from PML to surface
$q^*(\theta_{PML})$	Saturation specific humidity at the PML	—
q_{def}	Moisture input required to achieve saturation at the PML	$q^*(\theta_{PML}) - q_{mix}$
θ_{def}	Temperature increase required to reach θ_{BM}	$\theta_{BM} - \theta_{PML}$
ρz_{PML}	Column density from surface to PML	$\int_{z_{sfc}}^{z_{PML}} \rho dz$
ρz_{BCL}	Column density from surface to BCL	$\int_{z_{sfc}}^{z_{BCL}} \rho dz$
SH_{def}	Sensible heat necessary to reach the BCL	$c_p\left[\theta_{BM}\rho z_{BCL} - \int_{z_{sfc}}^{z_{BCL}} \theta(z)\rho dz\right]$
LH_{def}	Latent heat necessary to reach the BCL	$L\rho z_{PML} q_{def}$
MED	Minimum energy distance; minimum energy required to reach saturation	$\sqrt{(SH_{def})^2 + (LH_{def})^2}$
E_{adv}	Energy advantage; whether sensible or latent heat inputs favor saturation	$\arctan(LH_{def}/SH_{def})$
θ_{adv}	Potential temperature where the energy advantage transition occurs	Descend from $E_{adv} = 45$ to surface

partitioning in triggering convection over the SGP region, they simply highlight the difficulty of separating local from nonlocal impacts on convective initiation. Tawfik and Dirmeyer (2014) introduced the heated condensation framework (HCF) as a tool for addressing this issue. Using 40 yr of radiosonde observations and output from the NOAA Rapid Refresh forecast model, they demonstrated that HCF variables can be used to quantify how close the atmosphere is to triggering convection locally, thereby isolating the contribution of the atmospheric background state on convection initiation. The current study extends that work to describe the full suite of HCF variables and demonstrates the capability of them 1) to quantify the necessary moisture and heat inputs to trigger convection, 2) to identify the transition height separating the moistening advantage and boundary layer growth advantage regimes described by Gentine et al. (2013), 3) to identify which convective events were triggered locally, and 4) to point out sources of model bias in the convective state. These capabilities are demonstrated for a clear-sky and convectively active case over the ARM-SGP region in section 4, but first the HCF is detailed in section 2 and the datasets used are described in section 3. Section 5 provides a discussion of several points that emerged in the course of the study, and the summary and conclusions are given in section 6. A companion paper (Tawfik et al. 2015, hereafter Part II) applies the methodology presented here to the entire continental United States to evaluate the mean convective state and the nature of local convective initiation in relation to land–atmosphere coupling within a climatological context.

2. Heated condensation framework

The HCF contains a suite of variables that diagnose the current state of the atmosphere with respect to convection. These variables can be divided into two categories: 1) threshold variables and 2) evaluation variables that provide detailed information regarding the moisture and heat inputs required to trigger convection. It should be noted that evaluation variables are borne out of calculating the threshold variables. Only vertical profiles of potential temperature θ and specific humidity q are required to calculate the HCF variables. Both sets of variables are summarized in Table 1, and the method for calculating the full suite is described below.

a. Threshold variables

The buoyant condensation level (BCL) is defined as the level at which saturation would occur through buoyant mixing of heat and moisture alone as a result of heating at the surface. The BCL can also be regarded as the height the growing PBL needs to reach for saturation to occur without a change in total column moisture, only its vertical redistribution through complete mixing. In this regard the BCL is an intrinsic property of any profile, integrating information of column moisture and temperature in terms of buoyancy-driven convection.

To calculate the BCL, 2-m potential temperature θ_{2m} is increased by an increment $\Delta\theta$ mimicking surface heating, resulting in a new intermediate mixed layer, referred to as the potential mixed layer (PML) with a

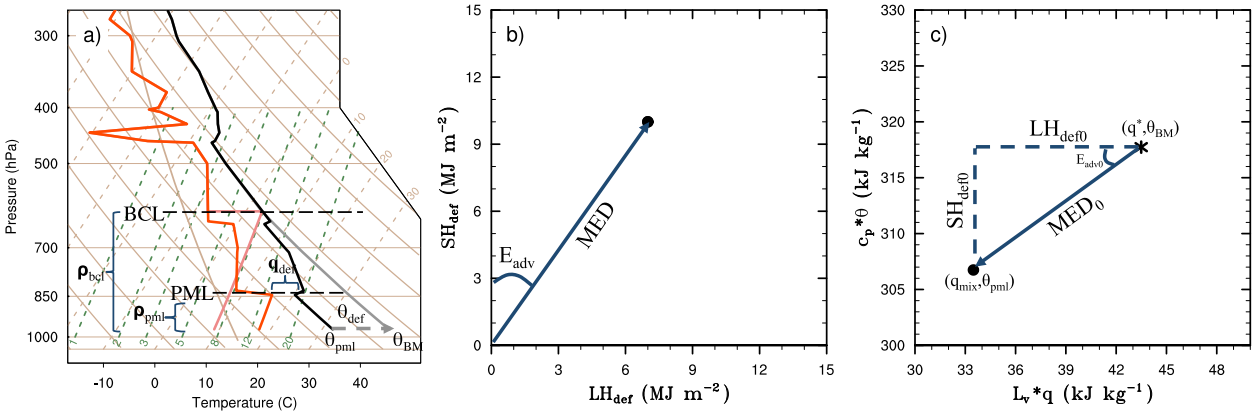

FIG. 1. (a) Thermodynamic profile (e.g., skew T–log$p$ diagram) describing variables needed to calculate the full HCF variable suite. See Table 1 for a summary of variable names and the text in section 2 for a full description. (b) Illustration of the relationship between $\mathrm{SH_{def}}$, $\mathrm{LH_{def}}$, MED, and E_{adv}. (c) Mapped HCF variables to mixing diagram space at the saturation point identified by the q^*, θ_{BM} pair (asterisk) and the PML identified by the q_{mix}, θ_{PML} pair (black dot). The zero subscript represents a modified energy deficit that is divided by the respective column density needed to convert from MJ m^{-2} to kJ kg^{-1}.

corresponding potential temperature θ_{PML} ($= \theta_{2\mathrm{m}} + \Delta\theta$). The specific humidity profile is then homogenized throughout the PML, returning a potential mixed layer specific humidity q_{mix}, which is compared to the saturation specific humidity at the top of the PML [$q^*(\theta_{\mathrm{PML}})$] to see if saturation occurs [specific humidity deficit q_{def}; $= q_{\mathrm{mix}} - q^*(\theta_{\mathrm{PML}})$, shown in Fig. 1a]. The BCL is reached on the condition that q_{def} equals zero. Note that θ_{BM} is the value of θ_{PML} once this condition is reached. Step-by-step details for calculating the two threshold variables BCL and θ_{BM} can be found in Tawfik and Dirmeyer (2014). The BCL and θ_{BM} are conserved quantities inherent to a given profile and do not require the arbitrary selection of a reference parcel, height, or layer of the atmosphere. This makes them powerful diagnostics for evaluating the departure from saturation for any given profile and allows for the direct comparison of convective preconditioning between observations and models.

b. Detailed evaluation variables

In addition to the threshold variables, terms can be calculated to evaluate specific attributes of a profile (cf. Table 1). The temperature deficit θ_{def} and specific humidity deficit (q_{def}) can be defined for every temperature increment describing, respectively, the surface temperature and moisture inputs needed in order for saturation to occur at the top of the mixed layer (Fig. 1a). Both terms approach zero as the BCL is reached. These deficit pairs can also be expressed as time-integrated flux values. To calculate the amount of additional latent heat energy necessary ($\mathrm{LH_{def}}$) for triggering convection, q_{def} is multiplied by the latent heat of vaporization L and the column density of the potential mixed layer ρz_{PML} (Fig. 1a). Similarly, the amount of additional sensible heat energy necessary ($\mathrm{SH_{def}}$) for triggering convection is calculated by subtracting the column-integrated sensible heat of the particular θ_{PML} profile [second term in Eq. (1)] from the total column-integrated sensible heat realized by the BCL [first term in Eq. (1)]:

$$\mathrm{SH_{def}} = c_p \theta_{\mathrm{BM}} \int_{z_{\mathrm{sfc}}}^{z_{\mathrm{bcl}}} \rho \, dz - c_p \int_{z_{\mathrm{sfc}}}^{z_{\mathrm{bcl}}} \theta(z) \rho \, dz, \qquad (1)$$

where c_p is the specific heat capacity of dry air, ρ is the air density of the particular profile (either the well-mixed BCL profile or the θ_{PML} profile; see Fig. 1a), and $\theta(z)$ is the potential temperature profile associated with a particular θ_{PML}. Note that $\mathrm{LH_{def}}$ represents the required moisture input needed to lower the BCL to intersect the PBL, whereas $\mathrm{SH_{def}}$ describes the additional sensible heat required to raise the surface temperature and grow the PBL to reach the BCL (i.e., in order to attain the θ_{BM} threshold; Fig. 1a). These two deficits can then be regarded as representing the surface-heating ($\mathrm{SH_{def}}$) and moisture-injection pathways ($\mathrm{LH_{def}}$) at a snapshot in time.

To identify the total energy departure from saturation and the relative importance of the energy components, $\mathrm{LH_{def}}$ and $\mathrm{SH_{def}}$ can be described in terms of vector quantities (Fig. 1b). The magnitude of the energy deficit vector, where $\mathrm{LH_{def}}$ is the x component and $\mathrm{SH_{def}}$ is the y component, describes the minimum energy distance (MED) needed to reach saturation, and the angle between the two components describes the degree of energy advantage E_{adv} (Fig. 1b). When E_{adv} is less than 45° the $\mathrm{LH_{def}}$ is less than the $\mathrm{SH_{def}}$, meaning

it is more advantageous, energetically, to add moisture to the PML rather than heat the surface and grow the PBL in order to reach saturation. The opposite holds for E_{adv} greater than 45°. Physically, the 45° line defines the transition from moistening advantage to dry advantage (i.e., boundary layer growth advantage). Note that this is similar to the mixing diagram formulation but evaluates the departure from saturation rather than absolute q and θ quantities; however, HCF variables can be mapped to mixing diagram space by simply eliminating the column density dependence ($SH_{def0} = c_p\theta_{def}$ and $LH_{def0} = Lq_{def}$), as is shown Fig. 1c. While it is not the focus of the current work, mapping HCF variables to mixing diagram space adds a straightforward quantification of saturation thresholds necessary for completing the soil moisture–precipitation feedback process chain and will be the subject of future work. Using this set of thresholds and evaluation diagnostics (Table 1), we can fully describe the state of the atmosphere with respect to convection in terms of time-integrated fluxes, as well as compare models and reanalysis directly against observations.

c. Comparison to parcel-derived quantities

Some of the HCF variables are analogous to parcel-derived variables commonly used to assess the likelihood of convective initiation. In particular the BCL is similar to the lifted condensation level (LCL), and the SH_{def} and θ_{def} are comparable to convective inhibition (CIN). The primary difference is that in the parcel theory framework parcels are assumed to ascend with some prescribed environmental entrainment rate. This entrainment rate has been the subject of many laboratory and numerical modeling studies (e.g., Stommel 1951; Morton et al. 1956; Squires and Turner 1962; Kuang and Bretherton 2006; Derbyshire et al. 2004; de Rooy et al. 2013; Matulka et al. 2014), whereas recent land–atmosphere coupling studies simply assume entrainment to be zero when calculating the LCL (e.g., Juang et al. 2007; Betts 2009; Ferguson et al. 2012; Couvreux et al. 2012; Santanello et al. 2013; Betts et al. 2014; Dirmeyer et al. 2014), artificially isolating the parcel from its environment. In this regard, both the need to select a parcel for ascent and to prescribe an entrainment rate result in additional degrees of freedom and consequently multiple possible LCL heights. Note that returning several LCL heights from a single atmospheric profile can be useful when evaluating maximum CAPE or possible cloud depths. However, with regard to convective initiation, it is well known that moist convection is not necessarily triggered when the LCL height, calculated from a single parcel, is lower than the PBL, making probabilistic ensemble plume approaches more appropriate (Golaz et al. 2002; Lawrence and Rasch 2005; Bogenschutz et al. 2012; D'Andrea et al. 2014).

On the other hand, HCF variables are inherent properties of the atmospheric column as they are constructed to mimic incremental buoyant mixing and observed boundary layer growth behavior and do not require parcel selection. Therefore, HCF variables are specifically suited for buoyancy-driven PBL regimes. For example, in order for CIN to be calculated, a level of free convection (LFC) must be present for a given parcel. The analogous HCF variables, SH_{def} and θ_{def}, do not have such a restriction, making them broadly applicable and column representative. Finally, because parcel-derived metrics are sensitive to the state variables of the chosen parcel, variables (like the LCL and CIN) derived from 2-m fields can vary dramatically throughout the diurnal cycle (Guichard et al. 2004). While this is advantageous when attempting to describe the temporal evolution of surface forcing on CAPE and cloud-top height, it makes it difficult to interpret how preconditioned the atmospheric background state is to convective triggering when comparing day to night. The potential complementary information arising from using parcel-derived metrics and the HCF are discussed further in section 5b. HCF variables change only when q and θ profiles evolve and are not especially sensitive to q and θ at a specific level. This is illustrated by the small change in estimated BCL height when degrading the number of atmospheric levels, which returns correlation coefficients R^2 greater than 0.9 and root-mean-square errors (RMSEs) of less than 0.6 km when reducing the observations to 29 and 20 levels for all ARM-SGP 1200 UTC soundings from 1994 to 2012.

3. Data

The current study demonstrates the ability of HCF variables to capture the convective state of the atmosphere over the ARM-SGP central site at Lamont, Oklahoma, during two contrasting cases from the International H2O Project (IHOP_2002; Weckwerth et al. 2004). The days were chosen to capture a completely clear-sky day (6 June, hereafter referred to as CLEAR) and a convectively active day over the central plains with local cloud cover and precipitation present (12 June, hereafter referred to as CLOUDY).

a. IGRA

Atmospheric soundings of temperature, humidity, pressure, and geopotential height necessary for computing HCF variables are retrieved from the Integrated

Global Radiosonde Archive (IGRA). The IGRA contains quality-controlled atmospheric profiles with most stations available from the 1970s to the present (Durre et al. 2006). Because the two days chosen for examination were during IHOP_2002 (Weckwerth et al. 2004), eight soundings are available for 6 June [~(0000, 0300, 0700, 0900, 1200, 1600, 1900, and 2100) local Central Daylight Time; CDT] and six for the 12 June case [~(0300, 0600, 0900, 1200, 1500, and 1800 CDT)]. All soundings during these two days had at least 33 vertical levels, with the exception of the 1800 CDT 12 June sounding, which had 16 levels.

b. ARM-BE

The ARM Best Estimate (ARM-BE; Xie et al. 2010) dataset provides a comprehensive suite of observations designed to capture the variables necessary for understanding cloud–radiation–surface interactions. Observed cloud fraction as a function of height from the Active Remote Sensing of Clouds (ARSCL) value-added product is used in the current work. The ARSCL contains best-estimate measurements from the millimeter-wavelength cloud radars (MMCRs), micropulse lidars (MPLs), and laser ceilometers. Hourly measurements from the ARSCL are available at 45-m vertical resolution with 512 levels starting at the surface. Precipitation, 2-m relative humidity, and 2-m temperature from ARM-BE are also used to provide a more complete portrait of clear-sky and convectively active case study days.

In addition to the observed variables, ARM-BE also packages output from the Rapid Update Cycle (RUC) model (Benjamin et al. 2004). The RUC is an operational forecast model that provides hourly forecasts at 13-km horizontal grid spacing and 37 vertical levels over the continental United States. Temperature, specific humidity, and geopotential height output from RUC are used to derive the full suite of HCF variables. The RUC model output and derived HCF variables are used to illustrate the ability for HCF variables to diagnose the nature of model biases in the convective state of the atmosphere. This helps show how the HCF can be used to guide model development and identify which characteristics pertaining to convective initiation are poorly captured by models.

c. NARR

The NARR is an extended regional data assimilation product that ingests surface observations every hour and atmospheric temperature, moisture, and wind every 3 h into the NCEP Eta Model (Mesinger et al. 2006). Assimilated precipitation is derived using daily totals from the National Climatic Data Center (NCDC) daily cooperative stations and Climate Prediction Center River Forecast Center stations that are then disaggregated into hourly totals using temporal weighted values from a 2.5° gridded analysis of hourly rain gauge data from the NCDC Hourly Precipitation Data stations over the continental United States where available. Global reanalysis precipitation is used where hourly gauge data are not available. The Noah land surface model is also run interactively within the assimilated system, returning internally consistent estimates of surface energy fluxes and soil moisture. The NARR provides output averaged over the prior 3 h on a Lambert conformal grid with approximately 32-km grid spacing over North America.

For the purposes of this study and to illustrate the ability of the HCF to pinpoint model biases in the atmospheric convective state, the NARR grid cell containing the ARM-SGP site was selected for the two case study days (6 and 12 June 2002). Three-hourly averaged temperature, specific humidity, and geopotential height profiles were retrieved from the NARR and used to calculate the full suite of HCF variables (Table 1). It should be noted that because NARR is a retrospective reanalysis, observed vertical profiles of temperature and humidity used to calculate HCF variables are likely assimilated. Therefore, biases are expected to be weaker in NARR relative to RUC, which is a 1-h forecast that would not be assimilating the observed profiles used for comparison.

4. Results

a. Case study description

During CLEAR the BCL was approximately 5.5 km high in the early morning and gradually increased to 6 km by 0700 CDT (Fig. 2a). Because this is an unattainable depth for the boundary layer to reach, convection due to local surface heating alone is not likely to occur. During the morning (0400 CDT) and early evening (2100 CDT) there were trace amounts of precipitation recorded at ARM-SGP (Fig. 2a). These trace precipitation totals may have been the result of morning fog or dew because the 2-m relative humidity (RH_{2m}) measured was close to 100% during these times, representing a shallow saturated layer near the surface (Fig. 2a). As the morning progressed, RH_{2m} decreased rapidly, typical of a growing mixed layer and surface heating (Betts 2009), and the convective initiation deficit θ_{def} never fell below 27 K (Fig. 2a)

The CLOUDY case has been the subject of many studies because of the intensive observational network deployed during this time (Weckwerth et al. 2004) and the

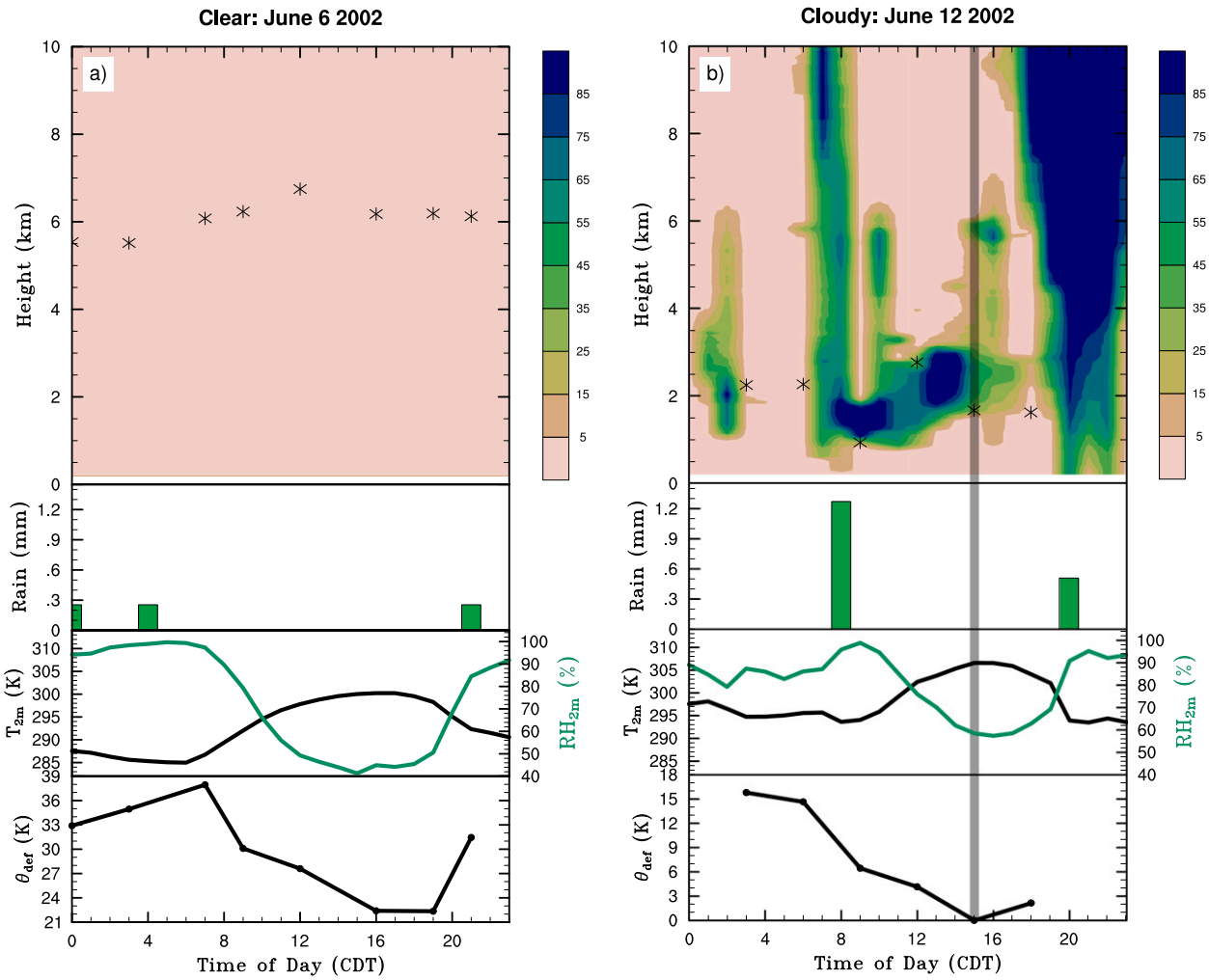

FIG. 2. Observed diurnal evolution of (from top to bottom) percent cloud cover (colored shading) and observed BCL height (asterisks), precipitation totals, 2-m temperature (black) with 2-m relative humidity (green), and potential temperature deficit for the (a) CLEAR and (b) CLOUDY cases. The vertical shaded area in (b) identifies locally triggered convection as calculated by the HCF ($\theta_{def} = 0$).

combination of complex mesoscale features (Markowski et al. 2006; Wilson and Roberts 2006; Weckwerth et al. 2008; Liu and Xue 2008). In particular, a mesoscale convective system (MCS) developed over central Kansas during the prior evening and propagated southeastward toward the ARM-SGP station, producing the deep cloud cover and 1.3 mm of precipitation at 0800 CDT (Fig. 2b). After the precipitation event, the BCL lowered from 2 to 1 km because of moistening of the column and surface (100% RH_{2m}; Fig. 2b). By late morning (1000–1200 CDT) low-level clouds thinned, allowing for some surface heating (seen as a 2-m temperature increase) and a corresponding drop in RH_{2M} (Fig. 2b). As detailed in prior work (Markowski et al. 2006; Liu and Xue 2008; Weckwerth et al. 2008), a residual outflow boundary that resulted from passage of the early morning MCS began to recede northward, advecting warm, moist air into the ARM-SGP observing region. This warm, moist air advection manifested in a lower BCL from 2.4 km at 1200 CDT to 1.8 km at 1500 CDT (Fig. 2b). By 1500 CDT, convection was initiated locally over the ARM-SGP facility, as identified by the HCF ($\theta_{def} = 0$; Fig. 2b, bottom), followed by an increased vertical extent in cloud cover from a 2.4-km to a 5.8-km maximum. This locally triggered event agrees with satellite imagery presented in prior work (e.g., Weckwerth et al. 2008). Thick, high clouds were then observed by 1700 CDT that subsequently evolved into a completely opaque cloud deck extending to the tropopause developed producing 0.5 mm of precipitation (Fig. 2b) due to a transient system originating to the west of the ARM-SGP facility (Weckwerth et al. 2008; Liu and Xue 2008). We can see that the complexity of the meso- and large-scale environments is captured by changes in the BCL height and θ_{def} over time

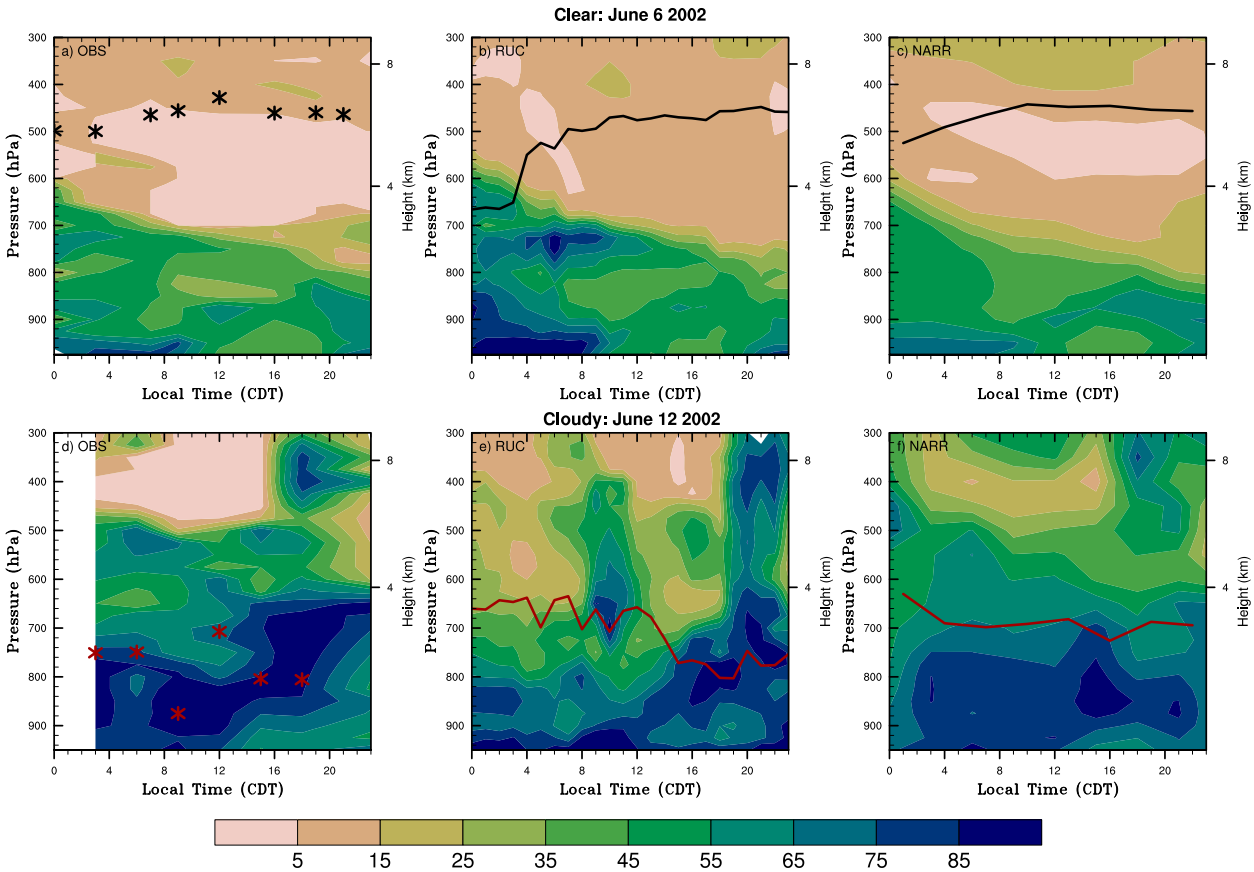

FIG. 3. Diurnal evolution of relative humidity (colored shading; %) profiles from (a),(d) observations; (b),(e) RUC; and (c),(f) NARR for the (top) CLEAR and (bottom) CLOUDY cases. The irregular lines and asterisks are the BCLs from models and observations, respectively.

at a single site. Locally triggered convection occurring over the ARM-SGP site and the related land–atmosphere coupling regimes (described by LH_{def}, SH_{def}, and E_{adv}) are elaborated upon in section 4d.

Figure 3 presents the diurnal evolution of the relative humidity profiles and BCL from observations (OBS), the RUC forecast model, and NARR datasets. Note that each of these datasets is sampled at different times and represents a range of spatial averaging (see section 3). For CLEAR, we find generally good agreement between OBS and the two models with regard to the diurnal evolution of the vertical structure of RH, with all datasets showing RH greater than 45% below 700 hPa and a dry layer (<15% RH) above 600 hPa (Figs. 3a–c). When comparing RUC to the OBS pattern, however, we see that RUC exaggerates the vertical extent of the enhanced near-surface RH observed prior to 0400 CDT during CLEAR (Fig. 3b). This results in a lower BCL height (Fig. 3b). Not surprisingly, the NARR RH profile and diurnal evolution of the BCL more closely follow OBS during CLEAR (Fig. 3c).

For the CLOUDY case, the observed BCL varies between 700 and 880 hPa, corresponding to RH values greater than 65% before 1200 CDT (Fig. 3d). After 1200 CDT, when 2-m temperature begins to rise (Fig. 2b), RH values greater than 85% are observed around 800 hPa, with relatively drier conditions closer to the surface indicative of a well-mixed boundary layer (Fig. 3d). RUC has a less saturated air mass above 800 hPa until 1500 CDT, resulting in a higher BCL (approximately 665 hPa) than OBS (Fig. 3e), but begins to mirror OBS after 1500 CDT. The BCL in NARR is relatively constant at around 660 hPa during CLOUDY, and the NARR RH profile shows little change in the vertical structure throughout the day (Fig. 3f).

The larger discrepancies in the BCL found on CLOUDY are not surprising because the rapidly changing observed cloud cover and humidity would be difficult for models to reproduce, especially given the 3-h averaged NARR compared to the instantaneous OBS measurements.

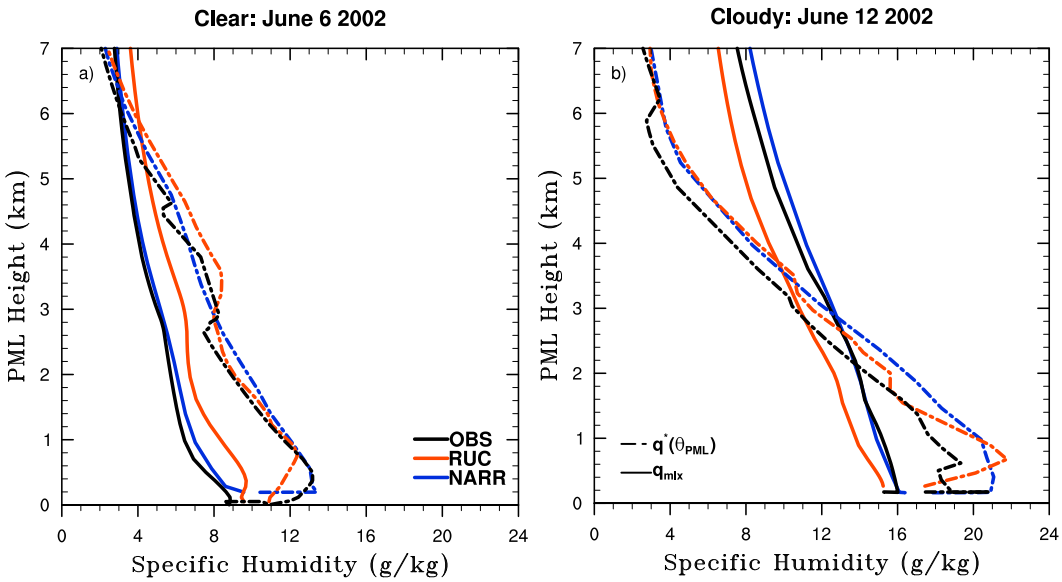

FIG. 4. Vertical profiles of potential mixed layer specific humidity (solid) and saturation specific humidity at the potential mixed level (dashed) from observations (black), RUC (orange), and NARR (blue) for the 1200 UTC morning soundings during the (a) CLEAR and (b) CLOUDY cases.

b. *Morning sounding: Temperature and mixed humidity*

Here the vertical profiles are dissected into their potential mixed layer specific humidity (q_{mix}) and potential mixed layer saturation specific humidity [$q^*(\theta_{\mathrm{PML}})$] components, allowing for biases in models and reanalysis to be examined in the context of convective triggering. This analysis is performed to show that while the convective triggering thresholds (BCL height and θ_{BM}) may be well represented, individual components contributing to saturation may have compensating biases, which may present the illusion of the models capturing the correct convective state, but this may be for the wrong reasons.

The morning sounding (1200 UTC) is selected for a more detailed examination because, outside of IHOP_2002 observational period, soundings are regularly launched at 1200 UTC, which is close to sunrise over much of the United States. Observed morning soundings are available at 0700 CDT for the CLEAR case and 0600 CDT for the CLOUDY case. Morning soundings from RUC are selected at the same hours and represent the average conditions of the prior hour. Because NARR is a 3-hourly averaged product, morning soundings refer to the 1200 UTC timestamp, which captures 0400–0700 CDT. The BCL is located at the height where $q^*(\theta_{\mathrm{PML}})$ intersects q_{mix}.

For the CLEAR day below 1 km, there is an inversion present for all datasets represented by the increase in $q^*(\theta_{\mathrm{PML}})$ with height (Fig. 4a). The OBS and NARR show stronger inversions with a maximum around 0.6 km, while RUC identifies a weaker inversion with a maximum at 0.9 km. The q_{mix} profiles exhibit a more gradual decrease with height from the surface to the BCL, with an expected maximum near the surface due to evapotranspiration (Fig. 4a). There is very good agreement in q_{mix} between OBS and NARR, especially above 2.5 km, while RUC tends to overestimate q_{mix} by approximately $2\,\mathrm{g\,kg^{-1}}$ throughout the entire profile (Fig. 4a). Despite having a moister profile, RUC still returns a slightly higher BCL. This is because of the higher $q^*(\theta_{\mathrm{PML}})$ found above 3 km that serves to increase q_{def} (Fig. 4a). Therefore, the wetter RUC moisture profile (higher q_{mix}) is compensated by a stronger environmental lapse rate reflected in $q^*(\theta_{\mathrm{PML}})$ generally returning the same BCL height as OBS, but due to compensating errors in temperature and moisture components (Fig. 4a).

For the CLOUDY case, q_{mix} is almost twice as high near the surface when compared to CLEAR (Fig. 4b). The OBS morning sounding shows a shallow inversion with rapid changes in $q^*(\theta_{\mathrm{PML}})$ at 0.2 km spanning a range of 17–21 $\mathrm{g\,kg^{-1}}$. RUC poorly represents the structure of $q^*(\theta_{\mathrm{PML}})$ by exaggerating the surface inversion and underestimates q_{mix} (Fig. 4b). This is the opposite bias found during CLEAR for RUC (Fig. 4a). Not surprising, NARR captures the q_{mix} profile very well below the BCL when compared to OBS, but overestimates $q^*(\theta_{\mathrm{PML}})$, resulting in a higher BCL than OBS (Fig. 4b).

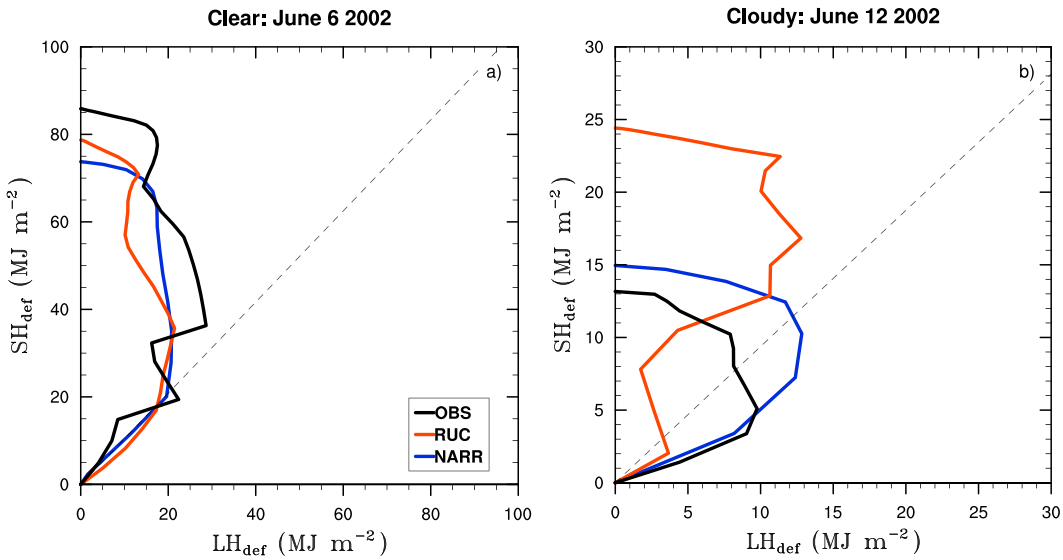

FIG. 5. LH_{def} and SH_{def} for the (a) CLEAR and (b) CLOUDY cases comparing energy deficit space for the morning soundings from observations (black), RUC (orange), and NARR (blue). The 1:1 line identifies the transition from moistening advantage regime ($SH_{def} > LH_{def}$) to the boundary layer growth regime ($SH_{def} < LH_{def}$).

c. *Morning sounding: Latent and sensible heat deficits*

The latent and sensible heat deficits (LH_{def} and SH_{def}), illustrated in Fig. 5 for the morning soundings (1200 UTC) on CLEAR and CLOUDY, quantify the amount of additional energy necessary for triggering convection through heating the surface (SH_{def}) or through additional moisture inputs (LH_{def}). The utility of this mixing-diagram-like energy space (Santanello et al. 2009) is that it poses convective initiation in terms of time-integrated flux unit. For example, an SH_{def} and LH_{def} pair of 20 and 10 MJ m^{-2}, respectively, means for a given mixed layer height (PML) it would take less latent heat energy input to trigger convection than to heat the surface (i.e., $LH_{def} < SH_{def}$). Therefore, more moisture is required to make surface heating a viable pathway for initiating convection relative to moisture inputs. This transition from moisture to PBL growth advantage is marked by the 1:1 line in Fig. 5. The unperturbed PML height (i.e., PML = PBL) corresponds to the highest SH_{def} values. Once no additional heating ($SH_{def} = 0$) or moistening ($LH_{def} = 0$) is needed convection is initiated; this is marked at the origin. Note that this differs from mixing diagram space in that energy deficits required to reach saturation are illustrated and that the change in these deficit diagnostics are described over time rather than describing the overall characteristics of the diurnal cycle.

The SH_{def} is approximately 3 times larger for the CLEAR morning sounding (74–86 MJ m^{-2}) when compared to CLOUDY (16–24 MJ m^{-2}; Fig. 5), meaning that less local surface sensible heating is required to reach the BCL during CLOUDY. This implies that the atmosphere is much drier during CLEAR and thus requires additional moisture, making latent heat inputs more energetically favorable for reaching saturation (represented by E_{adv} being mainly less than 45°). The behaviors of RUC and NARR are similar to OBS for the CLEAR sounding, with RUC showing a smaller LH_{def} resulting from the high q_{mix} biases shown in Fig. 4a.

The CLOUDY sounding again shows much greater variation between models and observations (Fig. 5b). The models have higher unperturbed (i.e., PML = PBL) SH_{def} (24 MJ m^{-2} for RUC and 15 MJ m^{-2} for NARR) than OBS (13 MJ m^{-2}). Additionally, the LH_{def} for the models is higher with both NARR and RUC, reaching a maximum around 13 MJ m^{-2} (Fig. 5b). Physically, this can be interpreted as NARR and RUC having less saturated atmospheres (Figs. 3d–f) and thus increasing the BCL height. More moisture is then required to lower the BCL height to intersect the PBL (i.e., a greater LH_{def}), and simultaneously greater heating is required to grow the PBL to intersect a now higher BCL (i.e., a greater SH_{def}). This cumulative effect represents the nonlinear relationship between the moisture and heat components involved in convective initiation, where a change in moisture results in a coincident response in the surface heating required to trigger convection. The implications for land–atmosphere coupling are discussed in section 5b.

d. *Diurnal evolution of convective state*

Through exploration of the diurnal evolution of the minimum energy distance (MED) and energy advantage

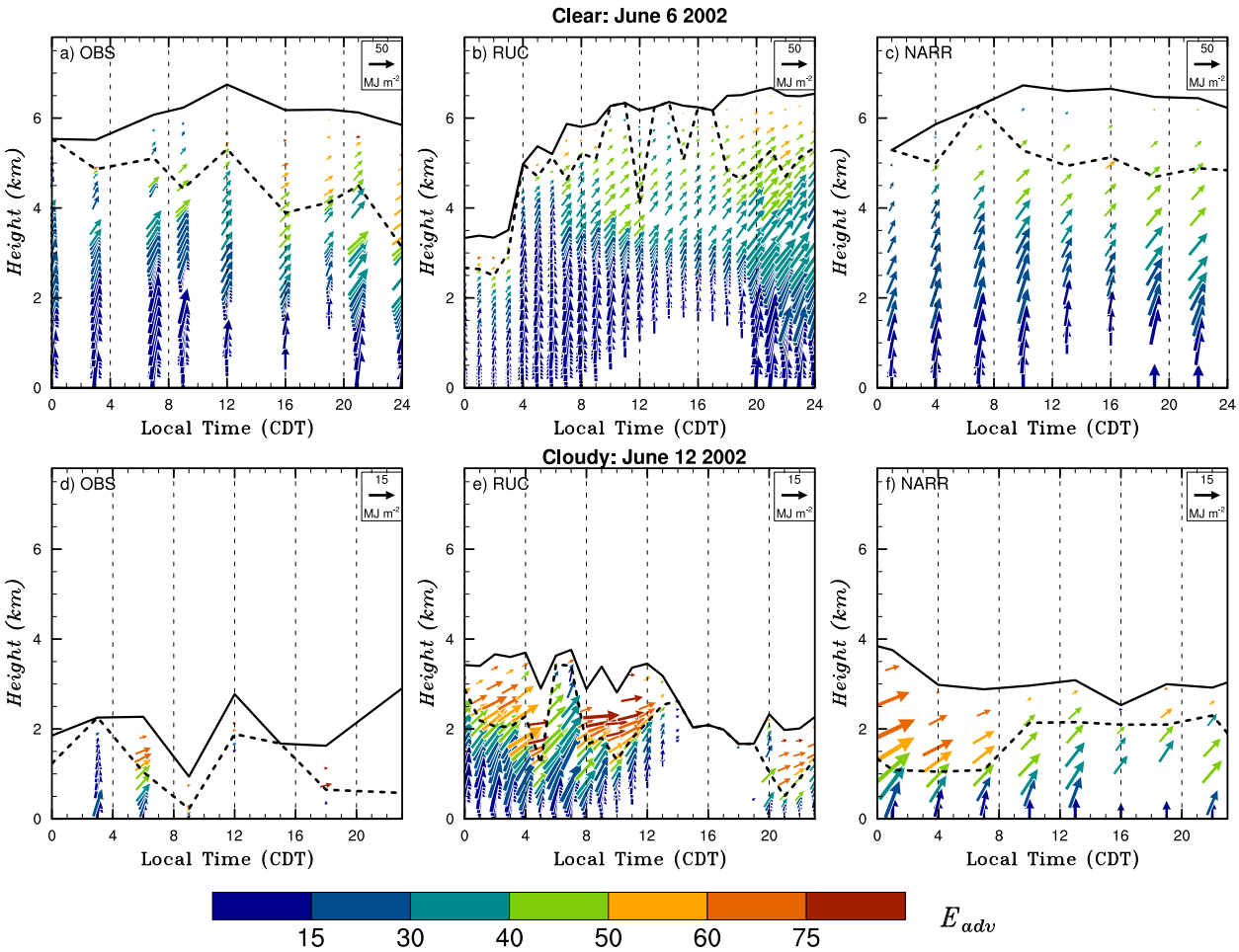

FIG. 6. Diurnal evolution of the vertical profile of the MED vectors (MJ m^{-2}) for (a),(d) observations; (b),(e) RUC; and (c),(f) NARR during the (top) CLEAR and (bottom) CLOUDY cases. The vectors are colored by the energy advantage regime where bluer colors represent a moistening advantage and redder colors represent a boundary layer growth advantage. The solid black line is the height of the BCL and the dashed line represents the energy advantage transition height ($E_{\mathrm{adv}} = 45$).

(E_{adv}) with height, the total energy required for convective initiation and relative energy deficits can be characterized. This will enable comparison between CLEAR and CLOUDY, with particular emphasis on the most energy advantageous pathway immediately prior to an observed local convective initiation event (CLOUDY at 1500 CDT; Fig. 2b). Figure 6 shows the diurnal cycle of the MED vector with height, where vectors are colored by E_{adv}, and MED approaches zero at the BCL. The green vectors represent the energy advantage transition. Note that CLEAR and CLOUDY cases have different reference magnitudes for the MED vectors because of the difference associated with relatively dry and wet soundings, respectively. Missing vectors below the BCL represent the boundary layer height as defined by the unperturbed PML height (e.g., $\theta_{\mathrm{PML}} = \theta_{2\mathrm{m}}$).

For both days MED is largest near the surface and decreases with height. The large MED near the surface is expected because $\mathrm{SH}_{\mathrm{def}}$ is largest when θ_{def} is maximized. The observed diurnal pattern of the transition height for CLEAR shows a higher energy advantage transition prior to 1200 CDT (~5 km) followed by a decrease (Fig. 6a). The RUC model, however, shows a 2-km increase in the transition height after 0300 CDT, and at times shows no transition at all, and thus remains in a moistening advantage regime (Fig. 6b). The NARR shows better agreement with OBS than the RUC, but fails to resolve the gradual decline of the transition height as the day progresses (Fig. 6c). The discrepancy in the transition height found in RUC after 0300 CDT corresponds to generally higher relative humidity below 650 hPa (Fig. 3b).

The CLOUDY case MED is less for the OBS than for NARR and RUC (Figs. 6d–f). This illustrates that less total energy is needed to reach saturation in the observations and the possibility of triggering convection

locally is higher. At 0300 CDT there is no observed transition height with the entire column below the BCL height in a moistening advantage regime (Fig. 6d). Both models do not capture this feature (Figs. 6e,f); however, from 0600 to 0700 CDT RUC does approach a completely moistening advantage regime (Fig. 6e). Although RUC has a much greater MED before noon during CLOUDY (Figs. 6e,f), RUC does capture the observed intersection of the PBL and BCL occurring at 1500 CDT (i.e., locally triggered convection). The NARR transition height is relatively shallow before 0700 CDT (~1 km) and stabilizes at 2 km for the remainder of the day, generally showing little variation, likely resulting from the NARR being a 3-hourly average product (Fig. 6f).

Overall, the MED vectors provide a good synthesis of the convective state of the atmosphere, providing information about 1) the total energy necessary for initiation, 2) the most advantageous energy pathway for achieving local convection, and 3) whether locally triggered convection was achieved. One of the greatest advantages, however, is that models and observations can be directly compared, requiring only standard atmospheric profiles and information at a single point to determine whether convection was locally triggered or transient in origin.

5. Discussion

Here we have applied the full suite of HCF threshold and evaluation variables (summarized in Table 1) to a clear-sky day (6 June; CLEAR) and a convectively active day (12 June; CLOUDY) during the IHOP_2002 campaign (Weckwerth et al. 2004). Observed convective conditions for CLEAR were characterized by 1) no cloud cover, 2) BCL higher than 5.5 km throughout the day, 3) 2-m relative humidity close to 100% prior to sunrise and a 50% drop by midday, 4) a moistening advantage regime near the surface with a transition zone to boundary layer growth advantage around 5 km, and 5) over 80 MJ m^{-2} of sensible heat needed to reach the BCL and trigger convection for most of the day. The CLOUDY day was characterized by 1) nonprecipitating cloud cover before sunrise followed by thicker cloud cover after sunrise; 2) two nonlocally originating MCS precipitation events, one immediately after sunrise and another prior to sunset; 3) a variable BCL from 1–3 km; 4) 2-m relative humidity above 60%; and 5) less than 15 MJ m^{-2} sensible heat needed to trigger convection, reaching zero (e.g., local convective initiation) by 1500 CDT. Overall, these characteristics demonstrate the ability of the HCF variables to represent the observed convective state of the atmosphere in terms of energy deficits and threshold behavior. Further discussion is provided here to place the model biases in perspective and to illustrate how the HCF can generally be applied to diagnose specific processes that are poorly represented. Additionally, comments are made regarding the initiation of local versus nonlocal convection and applications for assessing land–atmosphere coupling for each sounding.

a. Identifying model biases

The HCF can be used to diagnose model output and evaluate where the greatest biases in the convective background state lie. During the two case study days presented above, biases in the morning soundings were evaluated directly against observed soundings. We noted that RUC tended to have greater difficultly capturing the mixed humidity profile (q_{mix}) on the clear-sky (overestimate) and cloudy day (underestimate; Figs. 4a,b). This is despite capturing the BCL height fairly well for the clear-sky morning sounding (Fig. 4a). There were also biases in the saturation specific humidity profiles [$q^*(\theta_{\mathrm{PML}})$] found in RUC (Figs. 4a,b). The biases were most evident below 1 km and often poorly represented the strength and structure of the surface inversion (Figs. 4a,b). These biases become most apparent in the convective initiation threshold when it is lower, as was the case on 12 June. This suggests that the version of RUC in operation during these two days requires improvements in the vertical profiles of both specific humidity and saturation specific humidity, either through better assimilation or improved parameterizations; however, broader recommendations cannot be made based on these two case study days and are beyond the scope of this study. It should be noted that the RUC model has had many improvements since 2002, including increased horizontal and vertical resolution, improved assimilation, and dramatic changes to the base model (now the Rapid Refresh system since 1 May 2012; http://rapidrefresh.noaa.gov/). Therefore, while biases were pronounced during these two days, further analysis would be needed to assess the current state of the Rapid Refresh operational forecast system.

NARR, on the other hand, tended to represent the mixed humidity (q_{mix}) profile well, with biases only present in the temperature profile [$q^*(\theta_{\mathrm{PML}})$; Figs. 4a,b]. This is despite being a 3-hourly averaged product that was compared to instantaneous observations. The low q_{mix} biases are not surprising considering the assimilation of temperature and humidity profiles, and that special attention was dedicated to representing the hydrological cycle in NARR through the assimilation of precipitation. Precipitation was not assimilated directly but rather by imposing the necessary atmospheric latent

heat release associated with a particular amount of precipitation. This may be the cause of the higher saturation specific humidity bias found in the morning of the convectively active day. Additionally, Mesinger et al. (2006) showed that RMSEs in the NARR temperature profile tended to be highest near the surface when compared to rawinsondes. This suggests that improvements to the NARR convective state are best directed toward improving the structure and magnitude of the morning inversion during convectively active days through improving the surface energy fluxes and surface-layer parameterizations. A longer time series is required, however, to make a robust statement and recommendations for improving the convective states represented in NARR and RUC. Part II focuses on the climatological behavior over the contiguous United States, a portion of which is used to describe possible systematic biases present in the convective state of NARR.

b. *Energy advantage regimes*

The energy advantage (E_{adv}) calculated within the HCF identifies the most advantageous pathway, energetically, for initiating moist convection. When values of E_{adv} are less than 45°, it is more advantageous to inject moisture into the mixed layer to trigger convection (i.e., lower the BCL rather than heat the surface and grow the PBL to intersect the BCL). While this study does not directly assess the role of soil moisture and surface fluxes on moist convection, the amount of latent and sensible heat energy necessary for triggering convection is cast in the appropriate energy units ($\mathrm{J\,m^{-2}}$) needed to perform this type assessment. It should be noted that the moisture and boundary layer growth advantage regimes presented in this study are analogous to the wet and dry regimes identified in prior studies, respectively (Gentine et al. 2013; Westra et al. 2012; Findell and Eltahir 2003a), but with a few key differences.

As described by Gentine et al. (2013), the wet advantage refers to the ability for wetter soils to provide sufficient moisture to the atmosphere, thereby promoting convective initiation, whereas the dry advantage refers to the ability of drier soils to promote boundary layer growth leading to an increase in relative humidity at the top of the PBL. The main difference between the regimes presented here is that the moistening advantage ($E_{adv} < 45°$) is not exclusively attributable to local evaporation but may include moisture advection from nonlocal sources. Further, the moistening advantage described in this study is cast from the perspective of atmospheric demand, where E_{adv} defines the relative energy advantage and SH_{def}, LH_{def}, and MED provide the magnitude of energy needed. Additionally, it needs to be highlighted that the energy deficits used to calculate the advantage are tightly interrelated where an increase (decrease) in PBL moisture would simultaneously reduce (increase) LH_{def} and SH_{def}. The magnitude of change then determines the tendency of the energy advantage to change and depends largely on the depth of the mixed layer.

For the particular days examined, we note that during CLEAR the entire day was in a moistening advantage regime and approached but never achieved a boundary layer growth advantage when examining an unperturbed PBL (Fig. 6a). Physically this means that it is more advantageous to add moisture and lower the threshold (the BCL) rather than heat the surface and attempt to grow the PBL to intersect the current convective initiation threshold. Six days later during the CLOUDY case, we see that the BCL height did in fact lower by ~4 km (Fig. 2b) because of higher relative humidity (Fig. 3). This resulted in the only instances where the boundary layer growth advantage was observed. This occurred after 1200 CDT (Fig. 6b) when thin low-level clouds were present and was associated with local convective initiation (Fig. 2b).

While there are advantages of using the HCF, there is also complimentary information provided by the BCL–PBL comparison and the LCL deficit (LCL height minus PBL height; Santanello et al. 2011). When using 2-m fields to calculate the LCL height, the LCL deficit represents the degree to which the surface is forcing saturation at the top of the PBL. The BCL deficit (BCL height minus the PBL height), on the other hand, provides the departure from saturation at the top of the PBL. Together, these parameters may help identify the role of the surface forcing in triggering a particular event. Specifically, when the LCL deficit is negative (e.g., PBL reaches or exceeds the LCL) near-surface parcels tend to promote saturation throughout the PBL and are thereby acting to moisten the PBL. This surface-forced moistening would consequently lower the BCL. If the BCL were to be reached it can be said that saturation occurred, in part, because of local surface forcing where dissecting the relative contribution would require additional information from nonlocal moisture inputs (e.g., from advection). Conversely, if the LCL deficit is positive and the BCL deficit is zero (e.g., convective initiation), then surface drying contributed to growing the PBL to intersect the BCL. Therefore, combining these metrics may provide some insight into separating surface-forced manipulation of the BCL versus nonlocal influences. Quantifying the particular contribution is outside the scope of the current work, however.

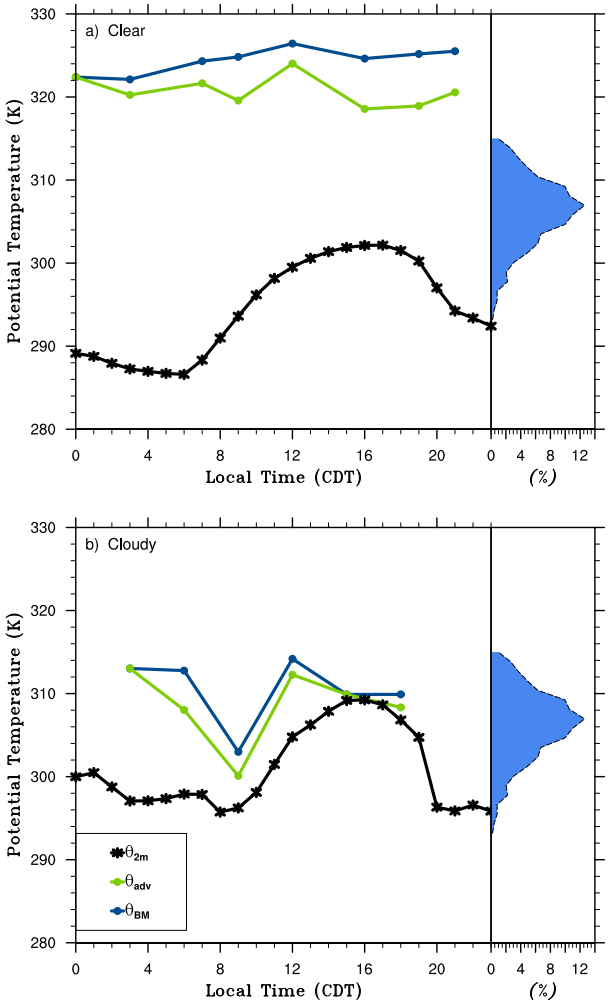

FIG. 7. Diurnal cycle of observed 2-m potential temperature (black), buoyant mixing potential temperature (blue), and potential temperature at the energy advantage transition (green) for the (a) CLEAR and (b) CLOUDY cases. The blue curve attached to the *y* axis is the sample probability distribution function of daily maximum 2-m potential temperature for all days in June from 1994 to 2012.

c. *Land–atmosphere coupling and convective initiation*

Throughout the clear-sky day there is a large separation between θ_{BM} and θ_{2m} (e.g., large θ_{def}) as well as a large separation between θ_{2m} and the potential temperature needed to reach the transition height (θ_{adv}; Fig. 7a). It is evident that θ_{2m} does not reach either of these thresholds during CLEAR. In this case the atmosphere requires more moisture to allow local convective initiation. The CLOUDY case has a cooler θ_{BM} threshold as well as a warmer θ_{2m} (Fig. 7b). This means convection is more likely to be triggered through local heating alone. Because intersection occurred at 1500 CDT, the CLOUDY day can be identified as having triggered convection locally. This approach (referred to as the retrospective method) for evaluating locally initiated convection can only be applied when convection actually occurs.

To quantify local land–convection interaction for hours when there is no convective initiation, climatological information of the daily maximum θ_{2m} can be used as an upper bound to see whether initiation is plausible. Specifically, the probability distribution of observed daily maximum θ_{2m} for all June months from 1994 to 2012 can be retrieved from ARM-SGP. When θ_{BM} is greater than any of the daily maximum θ_{2m} observed over the 19-yr record, there is a 0% chance of triggering convection for that particular hour according to the sample distribution. This means additional moisture is required to make convection viable for local convective initiation. When θ_{BM} lies within the bounds of the θ_{2m} distribution, it is plausible for local surface heating to trigger convection. The light blue curve in Fig. 7 reflects this 19-yr ARM-SGP sample distribution used to calculate the convective initiation probabilities. This method is referred to as the probabilistic method.

Applying this probabilistic method to CLEAR, we find that θ_{BM} and θ_{adv} fall well outside the maximum θ_{2m} distribution, and therefore convective initiation and a change in the energy advantage are very unlikely (Fig. 7a). The observed θ_{BM} for CLOUDY is much less and falls within the daily maximum θ_{2m} distribution. Therefore, convection is plausible during the CLOUDY case (Fig. 7b). This probability distribution method for quantifying convective likelihood is useful for quantifying convective initiation probabilities from observed soundings that may only be available twice a day but have a long-term hourly record of 2-m temperature and pressure. The retrospective and probabilistic approaches are used in Part II to assess summer (June–August) mean and interannual variability of convective initiation using observed morning soundings and NARR over the continental United States. One can imagine also applying knowledge of soil moisture states, environmental controls on Bowen ratio (e.g., by local vegetation), etc., to constrain the probabilistic approach that can then be applied to forecasting convection initiation.

6. Summary and conclusions

The heated condensation framework (HCF) introduced by Tawfik and Dirmeyer (2014) is elaborated upon, and the full suite of HCF variables are presented and applied to observations, reanalysis, and a forecast model data. The HCF variables provide a comprehensive way of assessing the convective state of the

atmosphere, and in particular isolate the influence of the large-scale background state on convective initiation. Because the HCF only requires atmospheric profiles of temperature and humidity to produce the entire suite of variables, models can be compared directly against observations, enabling a targeted model develop in relation to convection using the mixed humidity (q_{mix}) and the saturation specific humidity at the potential mixed level [$q^*(\theta_{\mathrm{PML}})$]. The utility and application of these diagnostics in evaluating the nature of the atmospheric convective state prior to initiation are illustrated for a clear-sky and a convectively active day.

Finally, the HCF can be used to evaluate whether local surface heating is capable of triggering convection. Convective initiation can be assessed in hindsight by identifying whether the BCL was reached during the day. This is not possible when there are only a few soundings during the day. However, the probability of initiating convection can be calculated if long-term daily maximum 2-m potential temperature data are available to compare against θ_{BM}. This has the advantage of quantifying the likelihood of triggering convection. The capabilities presented here enable a better process understanding of how the land surface may influence convective initiation, which can help improve convective triggering parameterizations going forward by using θ_{def} as an initiation criterion (Bombardi et al. 2015). Part II applies the HCF to the entire conterminous United States to explore the climatology and nature of convective initiation within the context of land–atmosphere coupling.

Acknowledgments. This work was supported by National Science Foundation Grant 0947837 for Earth System Modeling postdoctoral fellows. We thank Chiel van Heerwaarden for his excellent review and feedback, which greatly improved the methodology and quality of the manuscript.

REFERENCES

Benjamin, S. G., and Coauthors, 2004: An hourly assimilation–forecast cycle: The RUC. *Mon. Wea. Rev.*, **132**, 495–518, doi:10.1175/1520-0493(2004)132<0495:AHACTR>2.0.CO;2.

Berg, A., K. Findell, B. R. Lintner, P. Gentine, and C. Kerr, 2013: Precipitation sensitivity to surface heat fluxes over North America in reanalysis and model data. *J. Hydrometeor.*, **14**, 722–743, doi:10.1175/JHM-D-12-0111.1.

Betts, A. K., 1984: Boundary layer thermodynamics of a high plains severe storm. *Mon. Wea. Rev.*, **112**, 2199–2211, doi:10.1175/1520-0493(1984)112<2199:BLTOAH>2.0.CO;2.

——, 1992: FIFE atmospheric boundary-layer budget methods. *J. Geophys. Res.*, **97**, 18 523–18 531, doi:10.1029/91JD03172.

——, 2009: Land–surface–atmosphere coupling in observations and models. *J. Adv. Model. Earth Syst.*, **1,** doi:10.3894/JAMES.2009.1.4.

——, R. Desjardins, D. Worth, and B. Beckage, 2014: Climate coupling between temperature, humidity, precipitation, and cloud cover over the Canadian Prairies. *J. Geophys. Res. Atmos.*, **119**, 13 305–13 326, doi:10.1002/2014JD022511.

Bogenschutz, P. A., A. Gettelman, H. Morrison, V. E. Larson, D. P. Schanen, N. R. Meyer, and C. Craig, 2012: Unified parameterization of the planetary boundary layer and shallow convection with a higher-order turbulence closure in the Community Atmosphere Model: Single-column experiments. *Geosci. Model Dev.*, **5**, 1407–1423, doi:10.5194/gmd-5-1407-2012.

Bombardi, R. J., E. K. Schneider, L. Marx, S. Halder, B. Singh, A. B. Tawfik, P. A. Dirmeyer, and J. L. Kinter III, 2015: Improvements in the representation of the Indian summer monsoon in the NCEP climate forecast system version 2. *Climate Dyn.*, doi:10.1007/s00382-015-2484-6, in press.

Chaboureau, J. P., F. Guichard, J. L. Redelsperger, and J. P. Lafore, 2004: The role of stability and moisture in the diurnal cycle of convection overland. *Quart. J. Roy. Meteor. Soc.*, **130**, 3105–3117, doi:10.1256/qj.03.132.

Collier, J. C., and K. P. Bowman, 2004: Diurnal cycle of tropical precipitation in a general circulation model. *J. Geophys. Res.*, **109**, D17105, doi:10.1029/2004JD004818.

Couvreux, F., C. Rio, F. Guichard, M. Lothon, G. Canut, D. Bouniol, and A. Gounou, 2012: Initiation of daytime local convection in a semi-arid region analysed with high-resolution simulations and AMMA observations. *Quart. J. Roy. Meteor. Soc.*, **138**, 56–71, doi:10.1002/qj.903.

Dai, A., 2006: Precipitation characteristics in eighteen coupled climate models. *J. Climate*, **19**, 4605–4630, doi:10.1175/JCLI3884.1.

——, and K. E. Trenberth, 2004: The diurnal cycle and its depiction in the Community Climate System Model. *J. Climate*, **17**, 930–951, doi:10.1175/1520-0442(2004)017<0930:TDCAID>2.0.CO;2.

——, F. Giorgi, and K. E. Trenberth, 1999: Observed and model-simulated diurnal cycles of precipitation over the contiguous United States. *J. Geophys. Res.*, **104**, 6377–6402, doi:10.1029/98JD02720.

D'Andrea, F., P. Gentine, A. K. Betts, and B. R. Lintner, 2014: Triggering deep convection with a probabilistic plume model. *J. Atmos. Sci.*, **71**, 3881–3901, doi:10.1175/JAS-D-13-0340.1.

DeAngelis, A. M., A. J. Broccoli, and S. G. Decker, 2013: A Comparison of CMIP3 simulations of precipitation over North America with observations: Daily statistics and circulation features accompanying extreme events. *J. Climate*, **26**, 3209–3230, doi:10.1175/JCLI-D-12-00374.1.

Derbyshire, S. H., I. Beau, P. Bechtold, J. Y. Grandpeix, J. M. Piriou, J. L. Redelsperger, and P. M. M. Soares, 2004: Sensitivity of moist convection to environmental humidity. *Quart. J. Roy. Meteor. Soc.*, **130**, 3055–3079, doi:10.1256/qj.03.130.

de Rooy, W. C., and Coauthors, 2013: Entrainment and detrainment in cumulus convection: An overview. *Quart. J. Roy. Meteor. Soc.*, **139**, 1–19, doi:10.1002/qj.1959.

Dirmeyer, P. A., 2006: The hydrologic feedback pathway for land–climate coupling. *J. Hydrometeor.*, **7**, 857–867, doi:10.1175/JHM526.1.

——, 2011: The terrestrial segment of soil moisture–climate coupling. *Geophys. Res. Lett.*, **38**, L16702, doi:10.1029/2011GL048268.

——, R. D. Koster, and Z. Guo, 2006: Do global models properly represent the feedback between land and atmosphere? *J. Hydrometeor.*, **7**, 1177–1198, doi:10.1175/JHM532.1.

——, Z. Wang, M. J. Mbuh, and H. E. Norton, 2014: Intensified land surface control on boundary layer growth in a changing

climate. *Geophys. Res. Lett.*, **41**, 1290–1294, doi:10.1002/2013GL058826.

Durre, I., R. S. Vose, and D. B. Wuertz, 2006: Overview of the Integrated Global Radiosonde Archive. *J. Climate*, **19**, 53–68, doi:10.1175/JCLI3594.1.

Ek, M. B., and A. A. M. Holtslag, 2004: Influence of soil moisture on boundary layer cloud development. *J. Hydrometeor.*, **5**, 86–99, doi:10.1175/1525-7541(2004)005<0086:IOSMOB>2.0.CO;2.

Fennessy, M. J., and J. Shukla, 1999: Impact of initial soil wetness on seasonal atmospheric prediction. *J. Climate*, **12**, 3167–3180, doi:10.1175/1520-0442(1999)012<3167:IOISWO>2.0.CO;2.

Ferguson, C. R., and E. F. Wood, 2011: Observed land–atmosphere coupling from satellite remote sensing and reanalysis. *J. Hydrometeor.*, **12**, 1221–1254, doi:10.1175/2011JHM1380.1.

——, ——, and R. K. Vinukollu, 2012: A global intercomparison of modeled and observed land–atmosphere coupling. *J. Hydrometeor.*, **13**, 749–784, doi:10.1175/JHM-D-11-0119.1.

Findell, K. L., and E. A. B. Eltahir, 2003a: Atmospheric controls on soil moisture–boundary layer interactions. Part I: Framework development. *J. Hydrometeor.*, **4**, 552–569, doi:10.1175/1525-7541(2003)004<0552:ACOSML>2.0.CO;2.

——, and ——, 2003b: Atmospheric controls on soil moisture–boundary layer interactions. Part II: Feedbacks within the continental United States. *J. Hydrometeor.,* **4**, 570–583, doi:10.1175/1525-7541(2003)004<0570:ACOSML>2.0.CO;2.

——, P. Gentine, B. R. Lintner, and C. Kerr, 2011: Probability of afternoon precipitation in eastern United States and Mexico enhanced by high evaporation. *Nat. Geosci.*, **4**, 434–439, doi:10.1038/ngeo1174.

Frye, J. D., and T. L. Mote, 2010: The synergistic relationship between soil moisture and the low-level jet and its role on the prestorm environment in the southern Great Plains. *J. Appl. Meteor. Climatol.*, **49**, 775–791, doi:10.1175/2009JAMC2146.1.

Gentine, P., A. A. M. Holtslag, F. D'Andrea, and M. Ek, 2013: Surface and atmospheric controls on the onset of moist convection over land. *J. Hydrometeor.*, **14**, 1443–1462, doi:10.1175/JHM-D-12-0137.1.

Ghan, S. J., X. Bian, and L. Corsetti, 1996: Simulation of the Great Plains low-level jet and associated clouds by general circulation models. *Mon. Wea. Rev.*, **124**, 1388–1408, doi:10.1175/1520-0493(1996)124<1388:SOTGPL>2.0.CO;2.

Golaz, J.-C., V. E. Larson, and W. R. Cotton, 2002: A PDF-based model for boundary layer clouds. Part I: Method and model description. *J. Atmos. Sci.*, **59**, 3540–3551, doi:10.1175/1520-0469(2002)059<3540:APBMFB>2.0.CO;2.

Guichard, F., and Coauthors, 2004: Modelling the diurnal cycle of deep precipitating convection over land with cloud-resolving models and single-column models. *Quart. J. Roy. Meteor. Soc.*, **130**, 3139–3172, doi:10.1256/qj.03.145.

Guo, Z., and Coauthors, 2006: GLACE: The Global Land–Atmosphere Coupling Experiment. Part II: Analysis. *J. Hydrometeor.*, **7**, 611–625, doi:10.1175/JHM511.1.

Hohenegger, C., and B. Stevens, 2013a: Controls on and impacts of the diurnal cycle of deep convective precipitation. *J. Adv. Model. Earth Syst.*, **5**, 801–815, doi:10.1002/2012MS000216.

——, and ——, 2013b: Preconditioning deep convection with cumulus congestus. *J. Atmos. Sci.*, **70**, 448–464, doi:10.1175/JAS-D-12-089.1.

——, and ——, 2013c: Reply to "Comments on 'Preconditioning deep convection with cumulus congestus.'" *J. Atmos. Sci.*, **70**, 4155–4156, doi:10.1175/JAS-D-13-0216.1.

Juang, J.-Y., A. Porporato, P. C. Stoy, M. S. Siqueira, A. C. Oishi, M. Detto, H.-S. Kim, and G. G. Katul, 2007: Hydrologic and atmospheric controls on initiation of convective precipitation events. *Water Resour. Res.*, **43**, W03421, doi:10.1029/2006WR004954.

Koster, R. D., and Coauthors, 2004: Regions of strong coupling between soil moisture and precipitation. *Science*, **305**, 1138–1140, doi:10.1126/science.1100217.

——, and Coauthors, 2006: GLACE: The Global Land–Atmosphere Coupling Experiment. Part I: Overview. *J. Hydrometeor.*, **7**, 590–610, doi:10.1175/JHM510.1.

——, S. D. Schubert, and M. J. Suarez, 2009: Analyzing the concurrence of meteorological droughts and warm periods, with implications for the determination of evaporative regime. *J. Climate*, **22**, 3331–3341, doi:10.1175/2008JCLI2718.1.

Kuang, Z., and C. S. Bretherton, 2006: A mass-flux scheme view of a high-resolution simulation of a transition from shallow to deep cumulus convection. *J. Atmos. Sci.*, **63**, 1895–1909, doi:10.1175/JAS3723.1.

Lawrence, M. G., and P. J. Rasch, 2005: Tracer transport in deep convective updrafts: Plume ensemble versus bulk formulations. *J. Atmos. Sci.*, **62**, 2880–2894, doi:10.1175/JAS3505.1.

Lee, M.-I., I. Choi, W.-K. Tao, S. D. Schubert, and I.-S. Kang, 2010: Mechanisms of diurnal precipitation over the US Great Plains: A cloud resolving model perspective. *Climate Dyn.*, **34**, 419–437, doi:10.1007/s00382-009-0531-x.

Liang, X.-Z., 2004: Regional climate model simulation of summer precipitation diurnal cycle over the United States. *Geophys. Res. Lett.*, **31**, L24208, doi:10.1029/2004GL021054.

Lintner, B. R., P. Gentine, K. L. Findell, F. D'Andrea, A. H. Sobel, and G. D. Salvucci, 2013: An idealized prototype for large-scale land–atmosphere coupling. *J. Climate*, **26**, 2379–2389, doi:10.1175/JCLI-D-11-00561.1.

Liu, H., and M. Xue, 2008: Prediction of convective initiation and storm evolution on 12 June 2002 during IHOP_2002. Part I: Control simulation and sensitivity experiments. *Mon. Wea. Rev.*, **136**, 2261–2282, doi:10.1175/2007MWR2161.1.

Markowski, P., C. Hannon, and E. Rasmussen, 2006: Observations of convection initiation "failure" from the 12 June 2002 IHOP deployment. *Mon. Wea. Rev.*, **134**, 375–405, doi:10.1175/MWR3059.1.

Matulka, A., P. López, J. M. Redondo, and A. Tarquis, 2014: On the entrainment coefficient in a forced plume: Quantitative effects of source parameters. *Nonlinear Processes Geophys.*, **21**, 269–278, doi:10.5194/npg-21-269-2014.

Mei, R., and G. Wang, 2012: Summer land–atmosphere coupling strength in the United States: Comparison among observations, reanalysis data, and numerical models. *J. Hydrometeor.*, **13**, 1010–1022, doi:10.1175/JHM-D-11-075.1.

Mesinger, F., and Coauthors, 2006: North American Regional Reanalysis. *Bull. Amer. Meteor. Soc.*, **87**, 343–360, doi:10.1175/BAMS-87-3-343.

Morton, B. R., G. Taylor, and J. S. Turner, 1956: Turbulent gravitational convection from maintained and instantaneous sources. *Proc. Roy. Soc. London*, **234A**, 1–23, doi:10.1098/rspa.1956.0011.

Rosa, D., and W. D. Collins, 2013: A case study of subdaily simulated and observed continental convective precipitation: CMIP5 and multiscale global climate models comparison. *Geophys. Res. Lett.*, **40**, 5999–6003, doi:10.1002/2013GL057987.

Ruiz-Barradas, A., and S. Nigam, 2013: Atmosphere–land surface interactions over the Southern Great Plains: Characterization from pentad analysis of DOE ARM field observations and NARR. *J. Climate*, **26**, 875–886, doi:10.1175/JCLI-D-11-00380.1.

Santanello, J. A., C. D. Peters-Lidard, S. V. Kumar, C. Alonge, and W.-K. Tao, 2009: A modeling and observational framework for diagnosing local land–atmosphere coupling on diurnal time scales. *J. Hydrometeor.*, **10**, 577–599, doi:10.1175/2009JHM1066.1.

——, ——, and ——, 2011: Diagnosing the sensitivity of local land–atmosphere coupling via the soil moisture–boundary layer interaction. *J. Hydrometeor.*, **12**, 766–786, doi:10.1175/JHM-D-10-05014.1.

——, ——, A. Kennedy, and S. V. Kumar, 2013: Diagnosing the nature of land–atmosphere coupling: A case study of dry/wet extremes in the U.S. southern Great Plains. *J. Hydrometeor.*, **14**, 3–24, doi:10.1175/JHM-D-12-023.1.

Seneviratne, S. I., and Coauthors, 2006: Soil moisture memory in AGCM simulations: Analysis of Global Land–Atmosphere Coupling Experiment (GLACE) data. *J. Hydrometeor.*, **7**, 1090–1112, doi:10.1175/JHM533.1.

——, T. Corti, E. L. Davin, M. Hirschi, E. B. Jaeger, I. Lehner, B. Orlowsky, and A. J. Teuling, 2010: Investigating soil moisture–climate interactions in a changing climate: A review. *Earth-Sci. Rev.*, **99**, 125–161, doi:10.1016/j.earscirev.2010.02.004.

Song, H., W. Lin, Y. Lin, A. B. Wolf, R. Neggers, L. J. Donner, A. D. Del Genio, and Y. Liu, 2013: Evaluation of precipitation simulated by seven SCMs against the ARM observations at the SGP site. *J. Climate*, **26**, 5467–5492, doi:10.1175/JCLI-D-12-00263.1.

Squires, P., and J. S. Turner, 1962: An entraining jet model for cumulo-nimbus updraughts. *Tellus*, **14A**, 422–434, doi:10.1111/j.2153-3490.1962.tb01355.x.

Stommel, H., 1951: Entrainment of air into a cumulus cloud. *J. Meteor.*, **8**, 127–129, doi:10.1175/1520-0469(1951)008<0127:EOAIAC>2.0.CO;2.

Tawfik, A. B., and A. L. Steiner, 2011: The role of soil ice in land–atmosphere coupling over the United States: A soil moisture–precipitation winter feedback mechanism. *J. Geophys. Res.*, **116**, D02113, doi:10.1029/2010JD014333.

——, and P. A. Dirmeyer, 2014: A process-based framework for quantifying the atmospheric preconditioning of surface-triggered convection. *Geophys. Res. Lett.*, **41**, 173–178, doi:10.1002/2013GL057984.

——, ——, and J. A. Santanello, 2015: The heated condensation framework. Part II: Climatological behavior of convective initiation and land–atmosphere coupling over the conterminous United States. *J. Hydrometeor.*, **16**, 1946–1961, doi:10.1175/JHM-D-14-0118.1.

Taylor, C. M., R. A. M. de Jeu, F. Guichard, P. P. Harris, and W. A. Dorigo, 2012: Afternoon rain more likely over drier soils. *Nature*, **489**, 423–426, doi:10.1038/nature11377.

Trier, S. B., C. A. Davis, D. A. Ahijevych, and K. W. Manning, 2013: Use of the parcel buoyancy minimum ($B_{\min}$) to diagnose simulated thermodynamic destabilization. Part I: Methodology and case studies of MCS initiation environments. *Mon. Wea. Rev.*, **142**, 945–966, doi:10.1175/MWR-D-13-00272.1.

van Heerwaarden, C. C., J. Vilà-Guerau de Arellano, A. Gounou, F. Guichard, and F. Couvreux, 2010: Understanding the daily cycle of evapotranspiration: A method to quantify the influence of forcings and feedbacks. *J. Hydrometeor.*, **11**, 1405–1422, doi:10.1175/2010JHM1272.1.

Weaver, C. P., 2004: Coupling between large-scale atmospheric processes and mesoscale land–atmosphere interactions in the U.S. Southern Great Plains during summer. Part I: Case studies. *J. Hydrometeor.*, **5**, 1223–1246, doi:10.1175/JHM-396.1.

Weckwerth, T. M., and Coauthors, 2004: An overview of the International H_2O Project (IHOP_2002) and some preliminary highlights. *Bull. Amer. Meteor. Soc.*, **85**, 253–277, doi:10.1175/BAMS-85-2-253.

——, H. V. Murphey, C. Flamant, J. Goldstein, and C. R. Pettet, 2008: An observational study of convection initiation on 12 June 2002 during IHOP_2002. *Mon. Wea. Rev.*, **136**, 2283–2304, doi:10.1175/2007MWR2128.1.

Westra, D., G. J. Steeneveld, and A. A. M. Holtslag, 2012: Some observational evidence for dry soils supporting enhanced relative humidity at the convective boundary layer top. *J. Hydrometeor.*, **13**, 1347–1358, doi:10.1175/JHM-D-11-0136.1.

Wilson, J. W., and R. D. Roberts, 2006: Summary of convective storm initiation and evolution during IHOP: Observational and modeling perspective. *Mon. Wea. Rev.*, **134**, 23–47, doi:10.1175/MWR3069.1.

Xie, S., and Coauthors, 2010: ARM climate modeling best estimate data: A new data product for climate studies. *Bull. Amer. Meteor. Soc.*, **91**, 13–20, doi:10.1175/2009BAMS2891.1.

Zhang, G. J., 2003: Roles of tropospheric and boundary layer forcing in the diurnal cycle of convection in the U.S. Southern Great Plains. *Geophys. Res. Lett.*, **30**, 2281, doi:10.1029/2003GL018554.

Zhang, J., W.-C. Wang, and L. R. Leung, 2008: Contribution of land–atmosphere coupling to summer climate variability over the contiguous United States. *J. Geophys. Res.*, **113**, D22109, doi:10.1029/2008JD010136.

Zhang, Y., and S. A. Klein, 2010: Mechanisms affecting the transition from shallow to deep convection over land: Inferences from observations of the diurnal cycle collected at the ARM Southern Great Plains site. *J. Atmos. Sci.*, **67**, 2943–2959, doi:10.1175/2010JAS3366.1.

——, and ——, 2013: Factors controlling the vertical extent of fair-weather shallow cumulus clouds over land: Investigation of diurnal-cycle observations collected at the ARM Southern Great Plains site. *J. Atmos. Sci.*, **70**, 1297–1315, doi:10.1175/JAS-D-12-0131.1.